Producing 3-D Imitations of Soft Magnetic Composite Material Geometries

Joonas Vesa[1] and Paavo Rasilo[2]
[1,2]Unit of Electrical Engineering, Tampere University, Tampere, 33720 Finland

The main purpose of this paper is to describe a new algorithmic method to imitate 3-D geometries of soft magnetic composite materials. The method allows constructing various kinds of geometries for experimenting how certain geometric features affect different electromagnetic properties of the materials. Using the geometry imitations, we demonstrate that in order to explain the nonlinear static magnetic behaviour of certain composite, it is not necessary to assume contacts between neighbouring particles in the material. The contacts may instead be replaced by thin gaps.

***Index Terms*—B-H Curve, Geometry generation, Magnetic contact, Material identification, Soft magnetic composite, Voronoi tessellation.**

I. Introduction

SOFT magnetic composite (SMC) materials consist of small ferromagnetic particles, possibly coated with some electrical insulation material, compacted and heat treated. These kinds of materials have some significant advantages, *e.g.* isotropic behaviour in macroscopic scale and low eddy current losses since the conductivity between individual particles is relatively low [1], [2]. These qualities make the materials appealing for applications such as inductors and transformers. Manufacturing rotating electrical machines using SMC materials has also drawn much interest. This is partly due to reduced eddy currents and isotropic thermal and magnetic behavior. However, it has been suggested that the greatest benefit of using SMC materials in electrical machine cores comes from the manufacturing processes that can be simplified into few operations [3]. A microscope image of an SMC material is found in Fig. 1.

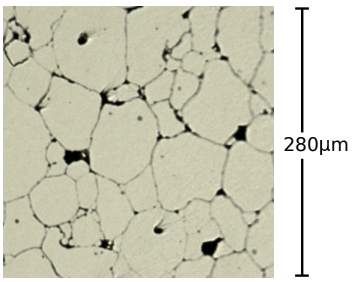

Fig. 1. A cross-section of a Fe-Ni-Mo alloy based SMC material.

The multiscale nature of SMC materials makes them tedious to model since some electromagnetic phenomena, like eddy currents, are strongly affected by the particle-size geometry. There are approaches for examining the particle-size structures. Cyr *et al.* proposed a two-dimensional approach based on meshing a real microscope image [4]. Similar kinds of approaches have been utilized later again [5]. Cyr's approach allows capturing geometric information about the materials. However, it was speculated that the assumption of two dimensionality might lead to inaccuracies in computational B-H curves. The study demonstrated that local saturation of the particles near the particle boundaries end up affecting the nonlinear effective permeability observed in the macroscopic scale.

This paper has two goals. The main goal is to introduce how imitations of soft magnetic composite geometries may be obtained in 3-D. Belkadi *et al.* proposed an algorithmic method to construct SMC material geometries in [6] and [7]. The algorithm was based on filling a regularly meshed reference cube by material and insulation regions. Our ideas are similar to the methods of Belkadi *et al.* in a general level. However, we aim at more clear definitions of different geometric parameters, such as particle contact surface areas and gap thickness variations, which we think would be very tedious to define using the methods of Belkadi due to the assumption of a regularly meshed geometry. Hence, we postulate another method to generate 3-D imitations of soft magnetic composite material geometries and to compute appropriate geometric parameters, like volume fractions, contact surface areas and gap thicknesses of the material geometries.

As soon as geometries can be obtained, we take one case-study that studies the nature of contacts between neighbouring particles in the material. In the literature, a term *magnetic contact* appears [5]. It was suggested that the linear magnetic permeability of an SMC, observed by macroscopic measurements, is easily underestimated if not considering magnetic contacts. However, we should be careful with the meaning of a magnetic contact since as soon as neighbouring particles are unified, the material becomes conductive. This could contradict the idea of SMC materials experiencing low conductivities. In [7] this problem was avoided by introducing magnetically conductive but electrically insulated regions between particles.

In our study we measure a static B-H curve of an SMC material. Then we postulate two different sets of geometries; one with neighbouring particles in contact and the other with neighbouring particles sharing thin gaps in between instead of contacts. We establish that the local B-H curves of the material particles may be estimated for these two sets in such a

Manuscript received January 14, 2019; revised June 6, 2019. Corresponding author: J. Vesa (https://tutcris.tut.fi/portal/en/persons/joonas-vesa(c7791107-71f3-413e-a85e-f8b4b7424509).html).

way that the computed effective B-H curves, that are observed in macroscopic scale, are in agreement with the measured one. The conclusion will be that the measured static B-H curve of the material may be explained without assuming contacts between neighbouring particles in the material. Demostrating this is the secondary goal of this paper. However, the inverse approach we use leaves open questions about the choices we make for the geometries. Uncertainties in the geometries lead to uncertainties in the estimated local B-H curves of the material particles. These open questions are briefly discussed at the end of this paper.

To be able to carry out the desired computations, some computational technicalities need to be covered shortly. In the computations we use a nonlinear single valued B-H curve for the material particles, which we estimate using a computational model against measurement data. Inverse methods for nonlinear magnetics have been studied by Sergeant [8] and Abdallh [9], [10] *et al*. The methods are based on expressing the local magnetic nonlinear permeability by some nonlinear trial function whose parameters are estimated by solving a least squares minimization problem. Our approach is similar but instead of using one trial function for the nonlinear permeability, we express the nonlinear part of the local B-H relation in a function basis.

It should be noted that algorithmic geometry generation has been studied quite extensively in the field of applied mechanics [11]. So far such treatment in the field of electromagnetics has received less attention.

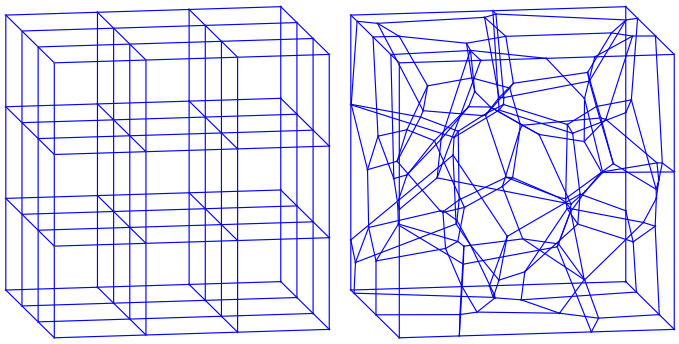

(a) Cubical tessellation (b) Voronoi tessellation

Fig. 2. Initially, a tessellation is formed for $[0, 1]^3$.

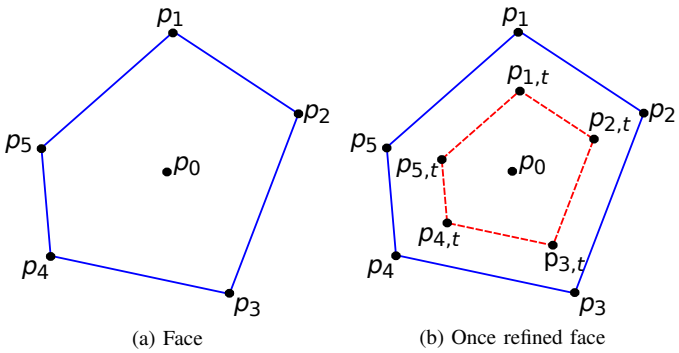

(a) Face (b) Once refined face

Fig. 3. (a) The point p_0 is an average of the vertices p_1,...,p_5. (b) The points $p_{i,t} = p_i + t\frac{p_0 - p_i}{\|p_0 - p_i\|}$, with $0 \leq t < 1$.

II. Geometries

In this section we describe the approach we have chosen for defining SMC-like geometries. All our codes have been implemented as Python codes.

A. Constructing geometries

Our approach is relatively simple. We begin with a spatial tessellation, refine the faces of each cell and then shrink the cells to obtain gaps and/or contacts between the cells. Finally, a boundary representation of the geometry is formed.

1) Tessellation

We begin with the cube $[0, 1]^3$ and perform a spatial tessellation for it to obtain a number N of cells. There are some restrictions for the chosen tessellation. Each cell of the tessellation is assumed to be a star domain with respect to the mean value of the cell's vertices. This is to ensure that shrinking the cell towards the mean value point does not occupy space outside the cell. Furthermore, each face of each cell is assumed to be a star domain with respect to the mean value of the face's vertices for the same reasons.

So far only cubical tessellation and Voronoi tessellation [12], [13] have been implemented, naturally the former being a special case of the latter. The motivation for cubical tessellations is simplicity and for Voronoi that the symmetry assumptions have been relaxed such that irregular geometries may be obtained. Also, the particle sizes may be randomized. We acknowledge that Voronoi diagrams are widely used to describe certain polycrystalline structures [14]. Voronoi tessellations are provided by PyVoro package and its backend Voro++ [15]. Voronoi diagrams may be viewed as a result of a ball-growth process from nucleation points who fully determine the diagram. If Voronoi tessellations are used, we set a positive real number d to denote the minimum distance between any two nucleation points and select the nucleation points randomly in the cube $[0, 1]^3$ under this condition. In Fig. 2 we see examples of both tessellations.

2) Refinement of the cell faces

Let us now consider an individual face of a cell in the tessellation. In Fig. 3a we see one such face, $[p_1, ..., p_5]$.

We define the point p_0 to be the mean of the vertices $p_1, ..., p_5$. Next, the face is refined by defining multiple contractions of the face $[p_1, ..., p_5]$ inside one another. In 3b, the vertices $p_1, ..., p_5$ are contracted towards p_0 by setting $p_{i,t} = p_i + t\frac{p_0 - p_i}{\|p_0 - p_i\|}$ using a predefined t with $0 \leq t < 1$. This defines another line loop, $[p_{1,t}, ..., p_{5,t}]$ inside $[p_1, ..., p_5]$. So far it makes no difference how the vertices $p_1, ..., p_5$ circulate, clockwise or counterclockwise, as long as the notation is consistent for each face.

Continuing this idea, one face can be further refined by adding more line loops inside the initial one. Such multiple refinements are defined by giving a collection of weights $w_F = [t_0, ..., t_k]$, with $t_i < t_j$ if $i < j$ and $0 \leq t_i < 1$ for each $i = 0, ..., k$. As a convention, we require $t_0 = 0$, which corresponds to the initial face. Hence, a refinement of the face

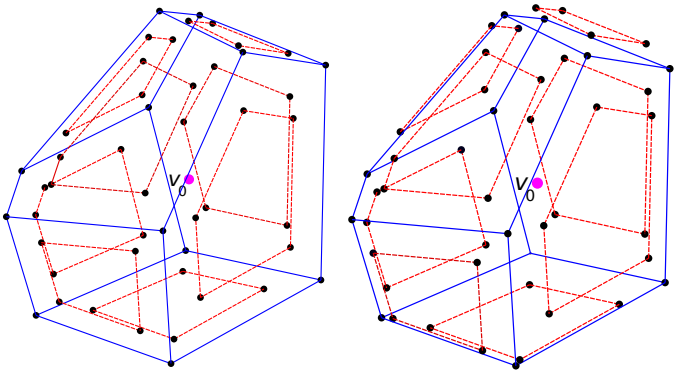

(a) Cell (b) Contracted cell

Fig. 4. (a) The purple point v_0 is an average of the vertices of the initial cell. (b) The points are moved towards v_0 by the formula $p_{i,t} = p_i + t\frac{v_0 - p_i}{\|v_0 - p_i\|}$, with $0 \leq t < 1$. In this picture, for the vertices in the solid blue faces $t = 0.1$ and they have been moved towards v_0. For the vertices in the dashed red faces $t = 0$ and they stay still.

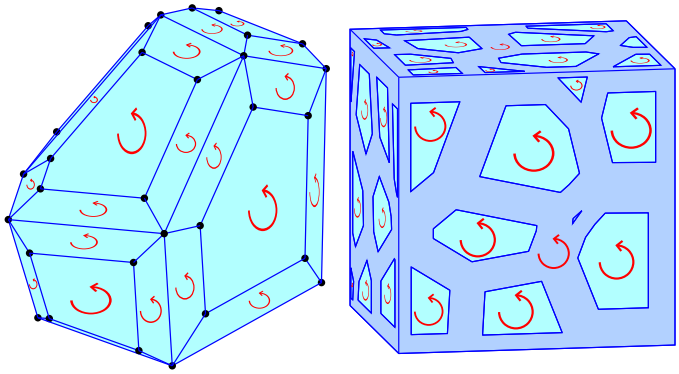

(a) Particle boundary (b) Cube boundary

Fig. 5. (a) Particle boundary is a chain of counter-clockwisely oriented surfaces. (b) Cube boundary is a chain of counter-clockwisely oriented planes that are such parts of particle boundaries that are lying on the boundary of the cube $[0, 1]^3$ and the the darker grey planes in the picture that are counter-clockwisely oriented planes with corresponding holes.

in Fig. 3a would be a collection $[[p_1, ..., p_5], [p_{1,t_1}, ..., p_{5,t_1}], ..., [p_{1,t_{k-1}}, ..., p_{5,t_{k-1}}], [p_{1,t_k}, ..., p_{5,t_k}]]$ with each line loop lying inside of the previous one in the list. For simplicity, in the schematic figures of this paper, we visualize only refinements consisting of just the initial line loops and one contracted loop inside each. However, in general, the refinement process accepts an arbitrary number of refined line loops.

The refinement process is carried out for every face of every cell in the tessellation. So far the parameter w_F is global in the sense that it defines refinements for each face similarly. We leave the possibility of defining and randomizing w_F separately for each face in the tesselation for future work.

3) Shrinking the particles

Fig. 4a illustrates one cell for which the face refinement, demonstrated in Fig. 3, has already been carried out. The solid blue lines in 4a describe the initial cell and the dashed red lines describe the contracted faces. The purple point v_0 is the mean of the vertices in the solid blue initial cell.

In Fig. 4b, the vertices in the solid blue faces are moved towards the point v_0 by the relation $p_{i,t} = p_i + t\frac{v_0 - p_i}{\|v_0 - p_i\|}$, with a predefined t under the condition $0 \leq t < 1$. The same procedure is repeated for the vertices in the dashed red faces also but with a different coefficient t.

Again, there might be any number k of layers given in the face refinement procedure, defined by w_F. Hence, we define a collection of coefficients $w_C = [t_0, ..., t_k]$, which corresponds to the coefficients w_F given in the previous section; the vertices of each contracted line loop, described by the coefficients w_F, are moved towards the mean v_0 by a corresponding weight in w_C. Setting some coefficients in w_C positive but less than one, one obtains gaps between particles and letting some coefficients equal to zero, leaves contacts between neighboring particles.

One generalization could be defined. In our setting, every particle is contracted by the same coefficients w_C. The possibility of defining and randomizing w_C individually for each particle remains for future work.

4) Constructing boundary representations

No computationally heavy geometric boolean operations such as unions and intersections of particles have to be considered when constructing a representation for the whole domain. This is a consequence of the particles and their faces being star domains in the initial tessellation as well as the definitions of the face refinement procedure and particle shrinking procedure. It follows that no particle occupies another particle's volume or volume outside the box $[0, 1]^3$. Instead, the geometry is expressed as formal linear combinations of geometric entities for which algebraic operations are well-defined. Such an approach serves two purposes. Firstly, it allows constructing the gap regions in a straight-forward manner using the information about the bounding box and the particles inside. Secondly, the approach produces a suitable structure for the geometry to be converted into a format required by an external meshing program.

First, we construct representations of the particles and their boundaries. In Fig. 5a we see one particle. Each plane in the boundary of the particle is considered as a counter-clockwisely ordered tuple of vertices. For instance, in Fig. 3b, one would be $[p_4, p_3, p_{3,t}, p_{4,t}]$. A particle is a tuple of planes who enclose the volume of the particle. In order to define the boundary of a particle, we have to express multiple oriented geometric entities at once. To do so, we use *chains*, formal linear combinations of geometric entities with integer coefficients. We define a boundary operator ∂ that returns for a particle a chain of its boundary planes with unit coefficients. Negative coefficients denote opposite orientations.

Next, we construct a representation for the gap region. In Fig. 5b we see the boundary of the bounding box which was earlier denoted as $[0, 1]^3$. This boundary is a chain of oriented planes in a similar manner than the boundaries of the particles are. Let us denote the boundary of the bounding box as b. If the particles are denoted as $p_1, ..., p_N$, the boundary of the gap regions g, denoted by ∂g, is given by

$$\partial g = b - \sum_{i=1}^{N} \partial p_i, \tag{1}$$

where ∂p_i stands for the boundary of the particle p_i. We define the gap g as a tuple of its boundary planes.

The whole space D is described by a formal linear combination

$$D = g + \sum_{i=1}^{N} p_i. \tag{2}$$

Defining boundary operators of different orders, and applying these boundary operators recursively beginning from D, we find all the lower dimensional entities such as planes and lines whose representatives are chosen on the run. This structure of entities of different dimensions and boundary operators between them is then converted into a Gmsh *geo*-file for meshing purposes [16]. In Fig. 6 we see the finished meshed geometries that are based on the tessellations in Fig. 2.

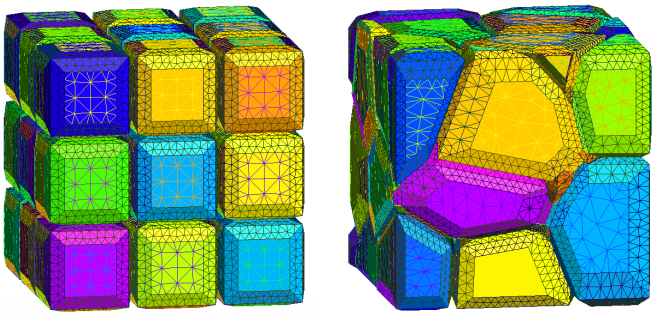

(a) Based on cubical tessellation (b) Based on Voronoi tessellation

Fig. 6. Selecting particle number $N = 27$, face contraction coefficients $w_F = [0, 0.4]$ and particle contraction coefficients $w_C = [0.1, 0]$ we get these meshed geometries. For visual reasons, the gap elements are left transparent. (a) A meshed periodical geometry with approximately 125000 elements and 16000 vertices. (b) A meshed irregular geometry. With Voronoi tessellations, an additional coefficient $d = 0.15$ was set to ensure minimum distance of 0.15 between any two distinct nucleation points. The mesh consists of approximately 150000 elements and 19000 vertices.

Gmsh admits some freedom for mesh density definitions. At the moment, we have defined a finer mesh density close to the particle edges. Our approach of defining geometries independently of meshes allows such optimizations.

5) Scaling

A scaling parameter is passed to the *geo*-file so that the volume of the meshed particle array can be set arbitrarily.

B. Geometric features

In this section we focus on introducing how to measure different geometric characteristics of the generated geometries.

1) Volumes and contact surfaces

We consider the total volume of the particles inside the box $[0, 1]^3$ as the volume fraction V_F of the geometry. This definition is independent of the later scaling of the geometry.

To measure contact surfaces between particles, let us consider again Fig. 4. Contracted cell (b) is contained inside cell (a). However, since the dashed red surfaces do not move, they form contacts between neighbouring particles. Contact surface fraction is defined by S_b/S_a, where S_b is the sum of the surface areas of the dashed red surfaces in 4b and S_a is the sum of the surface areas of the solid blue surfaces in 4a.

Next, we extend the definition of contact surface fraction to N particles with arbitrarily many face refinements. Define S_a to be the sum of all areas of the particle boundary surfaces in the geometry before the cells are shrinked by the process described in the subsection II-A3. Define S_b to be the sum of the areas of all the particle boundary surfaces of the geometry that do not move during the shrinking process. We denote the contact surface fraction S_b/S_a as S_F. The quantity S_F is scale independent.

2) Gap thickness characterization

The next task is to quantify the gaps between neighbouring particles. One thing we wish to measure is how the gap thickness varies over the geometry.

Let us consider one surface element of a particle after the refinement process of the particle faces but before the shrinking of the particles. One such surface element is $[p_4, p_3, p_{3,t}, p_{4,t}]$ in Fig. 3b. In Fig. 7 the same element is denoted by the darker purple surface found on the surface with the unit normal $\mathbf{n}_2$. During the shrinking process, the surface is transformed

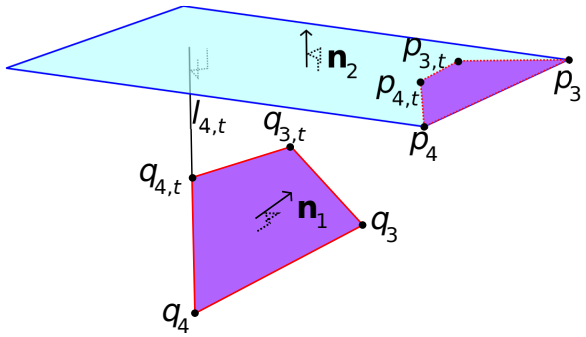

Fig. 7. A pair (A, l_i) is obtained by setting $A = (\mathbf{n}_1 \cdot \mathbf{n}_2)A^q/k$, where A^q is the area of the surface with unit normal $\mathbf{n}_1$ and l_i is the orthogonal distance between q_i and the plane with unit normal $\mathbf{n}_2$.

into $q := [q_4, q_3, q_{3,t}, q_{4,t}]$. Denote A^q as the area of the surface q and denote k as the number of vertices of the same surface and l_i as the orthogonal distance between q_i and the surface with unit normal $\mathbf{n}_2$. We define a pair (A, l_i), where A is a contribution of a projected surface area, given by $A = (\mathbf{n}_1 \cdot \mathbf{n}_2)A^q/k$. Intuitively, the pair can be interpreted such that an area of A can be found approximately from a distance l_i from the boundary of the initial tessellation. The coefficient $1/k$ allows summing A in a meaningful way over the vertex index i, resulting in the projection of A^q.

Let us now generalize the idea of measuring gaps into the case of arbitrary number of particles with arbitrarily refined faces and arbitrary shrinking of the particles. Similar kinds of pairs $(A_s, l_{s,v})$ may be defined for every vertex of every plane surface of each particle of the geometry, with s denoting a surface and v denoting a vertex in the surface s. In Fig. 7 one possible pair of indices would be $s = [q_4, q_3, q_{3,t}, q_{4,t}]$ and $v = q_{4,t}$. We define

$$L_{\text{avg}} = \frac{\sum_{s,v} A_s l_{s,v}}{\sum_{s,v} A_s} \tag{3}$$

to represent an area-weighted average of gap thickness portions. This does not define mean gap thickness between neighbouring particles, since we considered only the distances

between the faces of shrinked cells and the initial cells. However, this measure is quite enough to distinguish geometries with different gap shapes from each other. Further, we set

$$D_{\text{avg}} = \frac{\sum_{s,v} A_s |l_{s,v} - L_{\text{avg}}|}{\sum_{s,v} A_s} \tag{4}$$

to represent the absolute deviation of the weighted distances.

III. Computational methods

The primary objective of this paper, to automatically produce three dimensional imitations of soft magnetic composite geometries, has been introduced. Before we can study magnetic contacts and thin gaps, we must introduce some computational methods. This section contains technical details that are used in the computational study.

A. Formulation

The formulation is similar to [17] but in 3-D. Let us assume that a domain is given and necessary constitutive relations are defined in the domain.

Denote the domain with Ω. Assuming no eddy currents are present, the magnetic field $\mathbf{H}$ has a scalar potential. However, assuming a known excitation field $\mathbf{H}_{\text{ex}}$ under the condition $\nabla\times\mathbf{H}_{\text{ex}} = \nabla\times\mathbf{H} = \mathbf{0}$, we notice that $\mathbf{H}-\mathbf{H}_{\text{ex}}$ has a potential. Hence $\mathbf{H} = \mathbf{H}_{\text{ex}} + \nabla\varphi$, where $\mathbf{H}_{\text{ex}}$ is a known field and φ is an unknown scalar potential. Introducing the Gauss law for magnetism, the equation for the scalar potential becomes

$$\nabla \cdot \mathbf{B}(\mathbf{H}_{\text{ex}} + \nabla\varphi) = 0, \text{ in } \Omega, \tag{5}$$

where $\mathbf{B} = \mathbf{B}(\mathbf{H})$ is the constitutive relation.

We solve the equation for φ approximately by using the Galerkin finite element method with nodal scalar basis functions. We define $\mathbf{B}_{\text{avg}}$ and $\mathbf{H}_{\text{avg}}$ as $\mathbf{B}$ and $\mathbf{H}$ -fields averaged over Ω respectively. Setting

$$\varphi = 0, \text{ on } \partial\Omega,$$

it follows that $\nabla\varphi$ averages to zero and $\mathbf{H}_{\text{avg}}$ is just the average of the excitation field $\mathbf{H}_{\text{ex}}$. Furthermore we choose $\mathbf{H}_{\text{ex}}$ to be constant over Ω. The matter of interest is the nonlinear relation $\mathbf{B}_{\text{avg}}$-$\mathbf{H}_{\text{avg}}$, that is comparable to macroscale field measurements [17]. From now on, we denote $\|\mathbf{B}_{\text{avg}}\|$-$\|\mathbf{H}_{\text{avg}}\|$ as B_{avg}-H_{avg}.

B. Local constitutive model

Let us now relax the assumption of having explicitly defined the constitutive models. To define constitutive relations for the magnetizing particles, we use an inverse approach. We define the local constitutive model as a single-valued B-H relation so that its parameters may easily be estimated. Later, we use the computational formulation and optimize the parameters of the constitutive model such that measured B_{meas}-H_{meas} curves and computed B_{avg}-H_{avg} curves are in agreement.

We are going to define a scalar relation $B_{\text{sc}} = B_{\text{sc}}(\|\mathbf{H}\|)$ and extend it by isotropy by setting

$$\mathbf{B}(\mathbf{H}) = B_{sc}(\|\mathbf{H}\|)\frac{\mathbf{H}}{\|\mathbf{H}\|} \tag{6}$$

and $\mathbf{B} = \mathbf{0}$ if $\mathbf{H} = \mathbf{0}$. The question is how to define such scalar relation that has some extra freedom as parameters to be estimated.

To introduce an arbitrary number of degrees of freedom for the scalar relation without losing an intuitive interpretation of the parameters to be estimated, we proceed as follows. We write the scalar material relation as

$$B_{\text{sc}} = \mu_0 H_{\text{sc}} + J_{\text{sc}}, \tag{7}$$

where the scalar magnetic polarization J_{sc} is written in a suitable basis.

Consider increasing functions f_i, with $i = 1, ..., n$, such that $f_i(0) = 0$ and $\lim_{x\to\infty} f_i(x) = 1$. Let $J_{\text{sc}} = \sum_{i=1}^{n} \alpha_i f_i$. Setting constraints $\alpha_i \geq 0$, we find that J_{sc} is increasing, $J_{\text{sc}}(0) = 0$, and the saturation of J_{sc} is given by $J_{\text{sc,sat}} = \sum_{i=1}^{n} \alpha_i$. Our relation (7) reads as

$$B_{\text{sc}}(H_{\text{sc}}, \alpha) = \mu_0 H_{\text{sc}} + \sum_{i=1}^{n} \alpha_i f_i(H_{\text{sc}}). \tag{8}$$

This is just a collection of single valued material relations determined by the nonnegative coefficients $\alpha = [\alpha_1, ..., \alpha_n]$. Different kinds of choices could be made for the functions f_i. We choose very easy expressions for the functions f_i by setting

$$f_i(H_{\text{sc}}) = \begin{cases} -\left(\frac{H_{\text{sc}}}{H_{\text{sat},i}}\right)^2 + 2\frac{H_{\text{sc}}}{H_{\text{sat},i}}, & 0 \leq H_{\text{sc}} < H_{\text{sat},i} \\ 1, & H_{\text{sat},i} \leq H_{\text{sc}}, \end{cases}$$

where $H_{\text{sat},i}$ is just the value of magnetic field strength where the corresponding function f_i saturates. We chose four basis functions of this form demonstrated in Fig. 8.

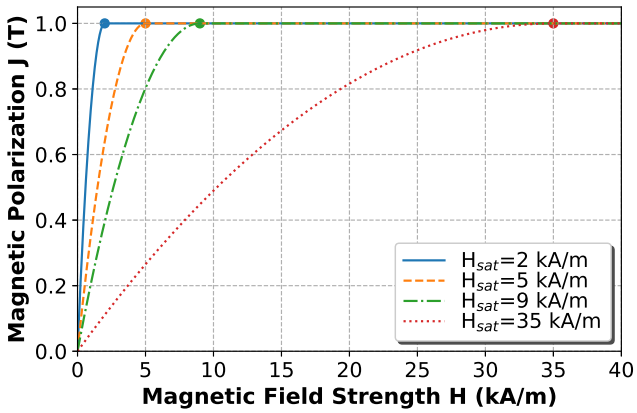

Fig. 8. Basis functions $f_1, ..., f_4$ are defined by choosing appropriate saturation points $H_{\text{sat},i}$ for each function. The saturation points are chosen heuristically by experimenting with different values.

Our α-dependent constitutive model for the magnetizing regions reads as $\mathbf{B} = \mathbf{B}(\mathbf{H}, \alpha)$ and for the gap regions we set $\mathbf{B} = \mathbf{B}(\mathbf{H}, 0)$.

C. Measurements

To choose the coefficients α, we perform an estimation against a measured B_{meas}-H_{meas} curve. Magnetics Inc.

C055106A2 MPP core [18] was chosen for a case-study. The microscope image in Fig. 1 was taken from such a toroid. In Fig. 9 we see a schematic image of the toroid in question.

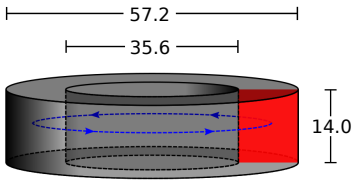

Fig. 9. Dimensions of the sample. The measures are expressed in millimetres. Red cross section is A = 144 mm^2. The corners were round in the original sample. The winding number of the primary coil was N_1 = 200 and for the secondary coil N_2 = 50. For simplicity, the length of the blue line may be approximated by l = 146 mm. Measurement frequency was 50 Hz.

A two-coil measurement setup was used. The primary winding was excited by sinusoidal 50 Hz voltage excitation while measuring the primary current $I(t)$ and the open-circuit secondary voltage $V(t)$. The magnetic flux through a cross section of the toroid, demonstrated by the red plane in Fig. 9, is given by

$$\Phi(t) = -\frac{1}{N_2}\int_0^t V(\tau)d\tau,$$

where N_2 is the number of turns in the secondary winding, $V(0)$ is assumed to be zero and $V(t)$ increasing around $t = 0$. We define B_{meas} by $B_{\text{meas}} = \Phi/A$, where A is represented by the area of the red plane in Fig. 9. Furthermore we set $H_{\text{meas}} = N_1 I/l$, where N_1 is the number of turns in the primary winding and l is represented by the length of the blue curve in Fig. 9.

In Fig. 10 we see the measured hysteresis loop. Consistently with the product catalog advertising these type of cores having low hysteresis losses [19], the measured loop shows negligible hysteresis. The loop is thus approximated by a single valued relation. We chose 35 measurement points from the positive part of the curve by choosing regular grids for both H and B axis and solving the corresponding intersections with the measured loop. These points are used later in the computations.

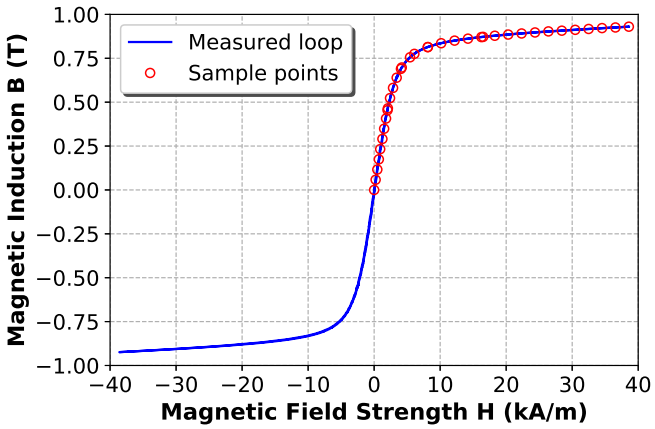

Fig. 10. Measured hysteresis loop and chosen B_{meas}-H_{meas} -samples.

D. Computational estimation

We use the scalar constitutive relation (8) with the chosen basis functions in Fig. 8 in the constitutive equation (6). We are denoting $(H_{\text{meas},i}, B_{\text{meas},i})$ with i=1, ..., n as the sampled measurements in Fig. 10. We express the excitation field in the formulation (5) in terms of the measurements as $\mathbf{H}_{\text{ex},i} = H_{\text{meas},i}\mathbf{e}_1$ with i denoting the i:th measurement sample. Using the Galerkin finite element method to compute the potential and averaging $\mathbf{B}$ over the domain, we find a relation $\mathbf{B}_{\text{avg}}(H_{\text{meas},i}, \alpha)$ that relates the averaged computational $\mathbf{B}_{\text{avg}}$ to the measured H_{meas} values. We wish to find such α that $\|\mathbf{B}_{\text{avg}}(H_{\text{meas},i}, \alpha)\|$ is close to $B_{\text{meas},i}$.

A cost function and constraints are defined by

$$\begin{aligned} r(\alpha) &:= \sum_{i=1}^{n}\Big(B_{\text{meas},i} - \|\mathbf{B}_{\text{avg}}(H_{\text{meas},i}, \alpha)\|\Big)^2, \\ \alpha_j &\geq 0, \;\; j = 1, ..., 4. \end{aligned} \tag{9}$$

We estimate the parameters α by finding a solution to the constrained minimization problem (9). Selecting an appropriate tolerance for the minimization problem, the agreement between the measured B_{meas}-H_{meas} and computed B_{avg}-H_{avg} is good, provided that the optimization converges. The optimizations are carried out using the Trust Region Reflective algorithm implemented in the Scipy optimization least squares package [20].

We set some terminology for the following computational study. There are three distinct B-H curves considered. Firstly, the curve B_{meas}-H_{meas} is called the *measured B-H curve*. Secondly, referring to the equation (8), the curve $B_{\text{sc}}(H_{\text{sc}}, \alpha)$-$H_{\text{sc}}$ is called the *estimated local B-H curve*. The curve depends on the parameter α, which is found by minimizing (9). Thirdly, the curve B_{avg}-H_{avg} is called the *computed effective B-H curve*, which depends on the estimated local curve.

IV. Computational Example

Let us now use the methods in one simple computational study. The aim of this study is to demonstrate that contacts of neighbouring particles in the material may be replaced by thin gaps without having to compromise the agreement between measured and computed effective B-H curves.

A. Choosing geometry parameters and the constitutive model

Using Voronoi tessellations and random nucleation points for the particles, we generate geometries with particle number $N = 27$, volume fraction $V_F = 0.9$ and contact surface fraction $S_F = 0.36$. Do these parameters correspond to the actual case-study material in Fig. 1? In this section, we discuss these chosen parameters as well as the local magnetic constitutive model of the particles.

Particle number N has to do with a choice of the representative cell of the material. A justification for N is given later by demonstrating that the results are similar if choosing much larger N instead of 27.

The volume fraction V_F may be approximated in two ways. One way is to turn the image in Fig. 1 into a two-color image.

Volume fraction is then determined by the fraction of the color representing the material. This was done for the material in Fig. 1 and $V_F \approx 0.899$ was found. However, this method is quite questionable, since any volume fraction may be obtained by choosing how the image is processed. Another approach is to compare the density 8 g/cm^3 given in the catalog [19] to the weighted mean of the densities of the constituents in the 81% nickel, 17% iron and 2% molybdenum alloy. This way we find a volume fraction $V_F \approx 0.91$. However, in this case it would be necessary to assume that the specific volumes of the constituents are preserved in the material. An approximation of $V_F = 0.9$ is chosen.

Finally, we choose the properties of the contact regions. We consider two cases; one with contacts in between the neighbouring particles and another with the contacts being replaced by thin gaps.

B. Geometries with contacts

As a reference, a contact surface fraction of $S_F = 0.36$ is chosen. To justify this could be a cumbersome task since the material becomes also conducting, which is contrary to the idea of SMCs. A practical point of view for such a choice can still be given; the contact surface fraction is chosen in a way that estimation of the local magnetic relation may be carried out such that the measured and computed effective B-H curves agree accurately. This of course does not validate S_F. It is merely a choice.

Chosen parameters N, V_F and S_F may be approximately obtained by setting the algorithm parameters, for instance $N = 27$, $d = 0.15$, $w_F = [0, 0.4]$, and $w_C = [0.1, 0]$. Here N is the number of particles in the reference cell, d denotes the minimum distance between the randomly placed N nucleation points, w_F defines how the cell faces are refined, and w_C defines how the cells are contracted. The parameters were further explained in Section II. Two hundred sample geometries were generated, and we call them *geometries with contacts*.

The next task is to estimate the local B-H relation for the particles. This procedure is carried out once, and then the same relation is used for all the other computations. Using one geometry, we perform an estimation of the local relation using the methods described in Section III-D. The optimization problem (9) yields parameters $\alpha = [1.1 \cdot 10^{-13}, 0.64, 0.36, 0.031]$ for the chosen values of $H_{\text{sat}} = [2, 5, 9, 35]\frac{\text{kA}}{\text{m}}$ to be used in the scalar constitutive model (8). The constitutive model with the chosen parameters H_{sat} and estimated values of α define the *estimated local* curve in Figure 11a. Using this estimated local B-H curve in the constitutive equiation (6), substituting to the formulation (5), solving the fields in the two hundred domains and averaging over the domains we find the two hundred curves, called *computed, 200 samples, contacts*, in Figure 11a. We call these curves the *computed effective* B_{avg}-H_{avg} curves. In the figures, the *measurement samples* are the same as in Fig. 10. In Fig. 11b we see the unsaturated region of the solutions given in Fig. 11a.

The agreement between the measured and the computed effective curves is considered good, since a cost less than

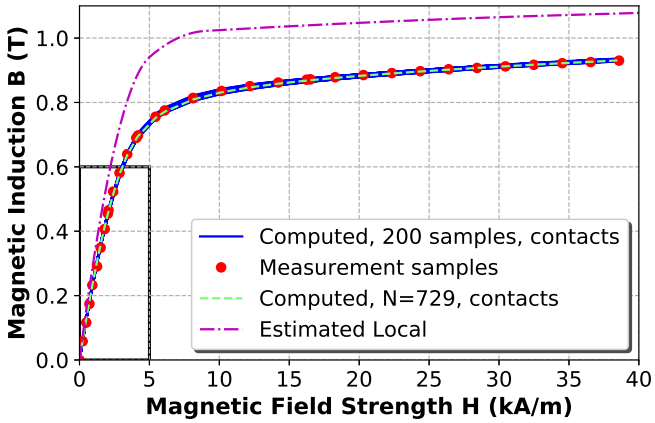

(a) Whole curve

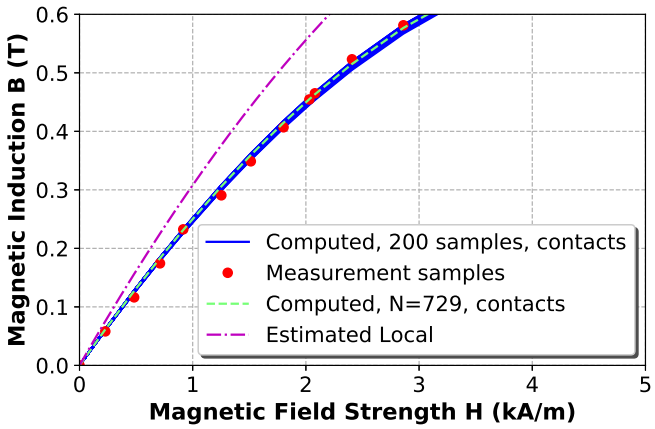

(b) Unsaturated part

Fig. 11. Computational results for samples with magnetic contacts as well as the measured B_{meas}-H_{meas} -curve and the estimated local B-H -curve.

$5 \cdot 10^{-4}$ T^2 of the cost function (9) was found by the estimation scheme of the local B-H curve. We also see that the two hundred computations yield consistent B_{avg}-H_{avg} even though the underlying initial Voronoi tessellation is randomized. There are major differences between the estimated local curve and the computed effective curves. This is due to the presence of gap regions in the domain. Since the measurements were carried out for the whole composite material, they are not useful in discussing whether the estimated local curve is meaningful or not. We will discuss this matter later in this paper by comparing the estimated local curve to another one obtained by using another type of geometry.

In Fig. 11a and 11b there is also an additional curve, obtained by a geometry with particle number $N = 729$. This represents a computation of B_{avg}-H_{avg} curve using the same local B-H relation as for the two hundred samples but with a geometry of 729 particles instead of 27. However, the parameters V_F and S_F are the same as well as the algorithm parameters w_F and w_C. Since the curve agrees with the computations by the two hundred sample geometries, we conclude that in this case it is enough to carry out computations using just 27 particles instead of 729. In Fig.

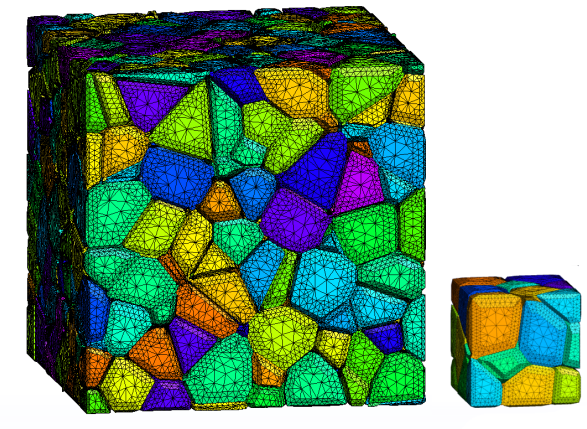

Fig. 12. A comparison between a geometry of 729 particles and 27 particles. The mesh of the geometry with 729 particles contains approximately 465 000 vertices and 2 700 000 elements.

12 we see images of the geometries of 729 particles and 27 particles.

C. Geometries with thin gaps

Let us now define another set of algorithm parameters, given by $N = 27$, $d = 0.15$, $w_F = [0, 0.4]$, and $w_C = [0.1, 0.001]$. Again, N is the number of particles in the reference cell, d denotes the minimum distance between randomly selected nucleation points, w_F defines how the cell faces are refined and w_C defines how the cells are contracted. The parameters were further explained in Section II. We generated two hundred such samples using randomized initial Voronoi tessellations, and we shall call them *geometries with thin gaps*.

The only difference between the geometries in this and in the previous section is the latter parameter of w_C. In this case the value is not zero but a small positive number. It means that in this case the contact surface fraction $S_F = 0$, all the particles are insulated and the contacts are replaced by thin gaps. The gap thickness characterization (3) yields an approximate distance $L_{\text{avg}} \approx 1.6 \cdot 10^{-4}$ for the regions that correspond to the contact regions in the previous section. Assuming this represents a half of the gap thickness of the non-scaled geometry and a scaling factor of $100\,\mu\text{m} : 1$, we find an approximate gap thickness of 32 nm. The volume fraction V_F is approximately the same 0.9.

As in the previous section, using one geometry, we performed an estimation of the local B-H relation using the methods described in Section III-D. The optimization problem (9) yields parameters $\alpha = [0.23, 0.7, 0.05, 0.041]$ for the chosen values of $H_{\text{sat}} = [2, 5, 9, 35]\frac{\text{kA}}{\text{m}}$ to be used in the scalar constitutive model (8). The constitutive model with the chosen parameters H_{sat} and estimated values of α define the *estimated local* curve in Figure 13a. Using this estimated local B-H curve in the formulation, solving the fields in the two hundred domains and averaging over the domains we find the computed effective B-H curves, called *computed 200 samples, thin gaps*, in Fig. 13a. In the figures, the *measurement samples* are just the same as in Fig. 10. A scaled version of the unsaturated region of the curves is found in Fig. 13b.

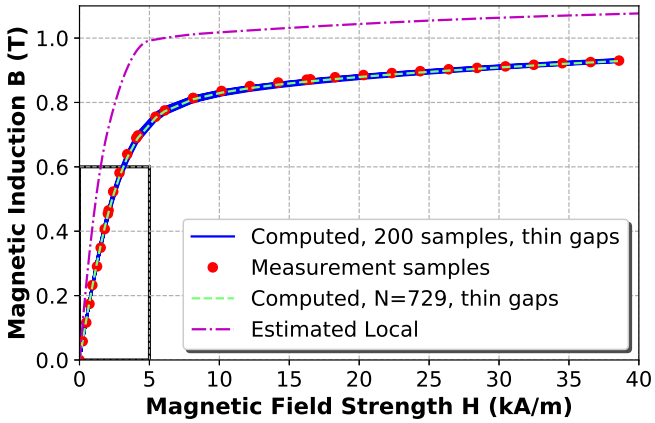

(a) Whole curve

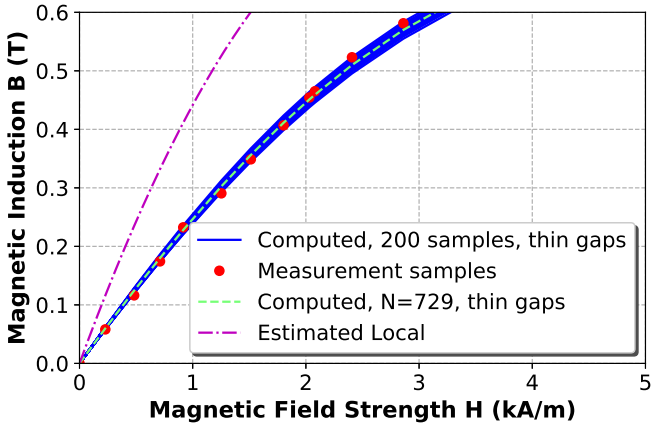

(b) Unsaturated part

Fig. 13. Computational results for samples with thin gaps as well as the measured B_{meas}-H_{meas} -curve and the estimated local B-H -curve.

A cost less than $5 \cdot 10^{-4}$ T^2 of the cost function (9) was found again and hence, the agreement between the measured and the computed curves is considered good. The two hundred computations yield consistent B_{avg}-H_{avg}. Again, there are major differences between the estimated local curve and the computed effective curves due to the presence of gap regions in the domain. The meaning of the local B-H curve is discussed later.

In Fig. 13a and 13b there is, again, an additional curve, obtained by a geometry with particle number $N = 729$ but the same parameters V_F, S_F, w_F and w_C as with the geometries with 27 particles. Since the curve agrees with the computations by the two hundred sample geometries, we say that also in this case it is enough to carry out computations using just 27 particles instead of 729.

D. Differences in the local magnetic relation

In the two previous sections we saw that the measured B_{meas}-H_{meas} relation may be repeated computationally using either the geometries with particles in contact or the geometries with particles sharing thin gaps in between instead of contacts. But in order to do so, we carried out estimations of

the local B-H relations of the particles once for both sets of geometries. Let us now compare the two estimated local B-H curves that were defined in Sections IV-B and IV-C.

In Fig. 14a we see a comparison of the two estimated local B-H curves, one of which was used in the computations using the geometries with contacts and the other using the geometries with thin gaps. In Fig. 14b the same results are visualized in a different scale to emphasize the differences.

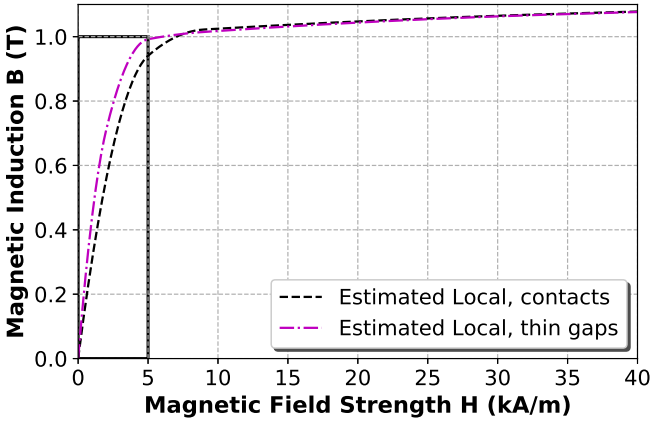

(a) Whole curve

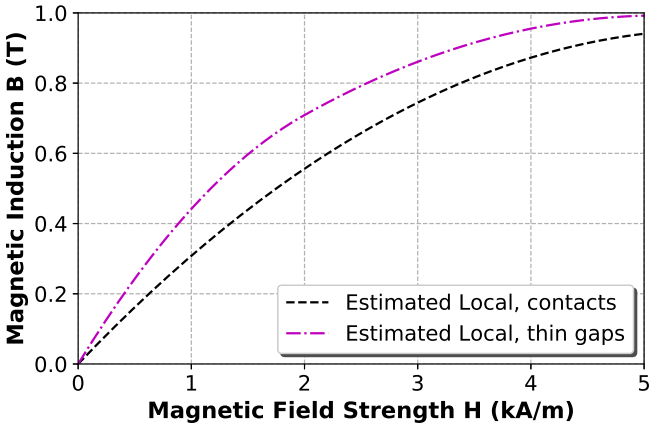

(b) Unsaturated part

Fig. 14. Estimated local B-H -curves for the two sets of geometries.

We see that the major differences in the estimated curves are in the unsaturated region of the curves framed in Fig 14a. In the case of geometries with contacts, we find the linear relative permeability of the estimated local B-H relation by differentiating (8). It yields $\mu_{\mathrm{r}} \approx 270$. On the other hand, for the geometries with thin gaps, the estimated curve yields a linear relative permeability of $\mu_{\mathrm{r}} \approx 420$. Both of the values are low compared to the values mentioned in [2] with sintered iron composites having relative permeabilities of several thousands and nickel dominated even tens of thousands.

We suspect that it is possible to find many more geometries that provide an agreement between measured and computed effective B-H curves observed in the macroscopic scale but with clear differences in the local linear permeabilities. To prefer one geometry over others, more measurement data needs to be gathered especially about the gaps between neighbouring particles in the material or the local magnetic behaviour of the material particles. This will be the focus in our further studies.

V. Conclusion

In this paper, we described a fairly simple method to construct 3-D geometries that imitate soft magnetic composite materials. The codes were written as python scripts that produce Gmsh geo-files that can later be used for meshing purposes. We conclude that automatic geometry generation is an efficient way of producing geometries by just choosing a few parameters. Also, the geometries can be randomized at least in terms of particle sizes. This approach allows experimentations on how different geometric parameters of the materials, such as volume fractions, contact surfaces and gap thickness variations, affect the electromagnetic properties of SMC materials. We acknowledge that even though the codes for automatized geometry generation reduce the manual labour of a researcher, computationally the problems can be very large.

In the second part of the paper, we considered two different sets of geometries. We generated two hundred geometries with equal particle number, volume fraction and contact surface fraction. It turned out that it was possible to estimate the local B-H curve of the material particles in such a way that the computed effective B-H curve of the case-study composite material and measurements were in agreement. Then we considered another set of two hundred geometries but this time contacts had been replaced by thin gaps. It turned out that through the same procedure of estimating the local B-H curve of the material particles it was possible to repeat computations of effective B-H curves that agreed well with the measurements. The conclusion is that in order to explain the static magnetization properties of an SMC material, it is not necessary to assume contacts in between neighbouring particles. Instead the contacts may be replaced by thin gaps, and yet the measurements can be explained.

It was established that there were clear differences in the unsaturated parts of the estimated local B-H curves of the material particles between the two sets of geometries. This suggests that there are unknown features in the produced geometries. To decide what kind of geometry imitation should be preferred over others, more measurements have to be brought in. Our future work concentrates on finding more information about the gaps and contacts in the case-study material by supplementary measurements.

In the future, the methods will be used in magnetodynamic simulations. Since SMC material geometries may be generated and meshed efficiently, the methods provide a way to study electromagnetic behaviour of such materials in realistic situations such as with rotating magnetic fields and nonsinusoidal excitations. This remains for future work.

Acknowledgment

The foundation of Emil Aaltonen and the Academy of Finland are acknowledged for financial support. The first author thanks his sister Saara for reading the paper and commenting on the style.

REFERENCES

[1] H. Shokrollahi and K. Janghorban, "Soft magnetic composite materials (SMCs)", *Journal of Materials Processing Technology*, vol. 189, Feb. 2007.

[2] K. Sunday, M. Taheri, "Soft magnetic composites: recent advancements in the technology", *Metal Powder Report*, vol. 72, no. 6, Nov./Dec. 2017.

[3] M. Persson, P. Jansson, A. G. Jack and B. C. Mecrow, "Soft Magnetic Composite Materials - Use for Electrical Machines", *IEE Conference Publication*, no. 412, 1995.

[4] C. Cyr, P. Viarouge, S. Clenet and J. Cros, "Methodology to Study the Influence of the Microscopic Structure of Soft Magnetic Composites on Their Global Magnetization Curve", *IEEE Transactions on Magnetics*, vol. 45, no. 3, Mar. 2009.

[5] Y. Ito, H. Igarashi, M. Suzuki, Y. Iwasaki and K. Kawano, "Effect of Magnetic Contact on Macroscopic Permeability of Soft Magnetic Composite", *IEEE Transactions on Magnetics*, vol. 52, no. 3, Mar. 2016.

[6] M. Belkadi, B. Ramdane, D. Trichet and J. Fouladgar, "Non Linear Homogenization for Calculation of Electromagnetic Properties of Soft Magnetic Composite Materials", *IEEE Transactions on Magnetics*, vol. 45, no. 10, Oct. 2009.

[7] M. Belkadi, D. Trichet, B. Ramdane and J. Fouladgar, "Modeling of Soft Magnetic Composite Material Using a Non Linear Homogenization Method", *Proc. CEFC*, Chigago, IL, USA, May 2010.

[8] P. Sergeant, G. Crevecoeur, L. Dupré, and A. Van den Bossche, "Characterization and optimization of a permanent magnet synchronous machine", *Int. J. Comput. Math. Elect. Electron. Eng.*, vol. 28, no. 2, 2009.

[9] A. Abou-Elyazied Abdallh, P. Sergeant, G. Crevecoeur, L. Vandenbossche, L. Dupré and M. Sablik, "Magnetic Material Identification in Geometries With Non-Uniform Electromagnetic Fields Using Global and Local Magnetic Measurements", *IEEE Trans. Magn.*, vol. 45, no. 10, Oct. 2009.

[10] A. Abou-Elyazied Abdallh and L. Dupré, "A Unified Electromagnetic Inverse Problem Algorithm for the Identification of the Magnetic Material Characteristics of Electromagnetic Devices Including Uncertainty Analysis: A Review and Application", *IEEE Trans. Magn.*, vol. 51, no. 1, Jan. 2015.

[11] Multiscale modelling and design for engineering application, *VTT Technology 77*, Kopijyvä Oy, Kuopio 2013.

[12] S. N. Chiu, D. Stoyan, W. S. Kendall, J. Mecke, *Stochastic Geometry and its Applications*, John Wiley & Sons, Ltd., 2013.

[13] A. Okabe, B. Boots, K. Sugihara, S. N. Chiu, *Spatial Tessellations*, John Wiley & Sons, Ltd., 2000.

[14] S. Falcoa, J. Jiang, F. De Cola, N. Petrinica, Generation of 3D polycrystalline microstructures with a conditioned Laguerre-Voronoi tessellation technique, *Computational Materials Science*, vol 136, Aug. 2017.

[15] C. H. Rycroft, "Voro++: A three-dimensional Voronoi cell library in C++", *Chaos; An Interdisciplinary Journal of Nonlinear Science*, vol. 19, Aug. 2009.

[16] C. Geuzaine, J.-F. Remacle, "Gmsh: a three-dimensional finite element mesh generator with built-in pre- and post-processing facilities," *International Journal for Numerical Methods in Engineering,* vol. 79, no. 11, 2009.

[17] I. Niyonzima, R. V. Sabariego, P. Dular, C. Geuzaine, "Finite Element Computational Homogenization of Nonlinear Multiscale Materials in Magnetostatics", *IEEE Transactions on Magnetics*, vol. 48, no. 2m Feb. 2012.

[18] Magnetics Inc. C055106A2 datasheet, Revision Nov. 2016, https://www.mag-inc.com/Media/Magnetics/Datasheets/C055106A2.pdf.

[19] Magnetics Inc. Powder Cores catalog 2017, https://www.mag-inc.com/Media/Magnetics/File-Library/Product%20Literature/Powder%20Core%20Literature/2017-Magnetics-Powder-Core-Catalog.pdf.

[20] Scipy scipy.optimize.least_squares documentation, Cited in Mar. 2018, https://docs.scipy.org/doc/scipy/reference/generated/scipy.optimize.least_squares.html#scipy.optimize.least_squares.